Journal of Energy Storage 128 (2025) 117220

Contents lists available at ScienceDirect

Journal of Energy Storage

journal homepage: www.elsevier.com/locate/est

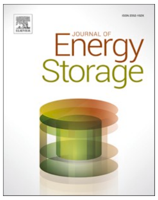

Research papers

Experimental study on thermal runaway characteristics and fire hazards of lithium-ion batteries in semi-confined space of transportation

Lulu Song [a,1], Zhizuan Zhou [a,1], Xiaoyu Ju [a,*], Boxuan Wang [a], Ulises Rojas-Alva [b], Xiaodong Zhou [a], Lizhong Yang [a,*]

[a] State Key Laboratory of Fire Science, University of Science and Technology of China, Hefei, Anhui, China
[b] Department for Fire-Safe Sustainable Built Environment (FRISSBE), Slovenian National Building and Civil Engineering Institute (ZAG), Logatec, Slovenia

ARTICLE INFO

Keywords:
Lithium-ion batteries
Transportation safety
Thermal runaway
Fire hazard

ABSTRACT

Fire incidents involving lithium-ion batteries during transportation have become increasingly frequent, causing significant property damage and posing serious health risks to individuals nearby. Despite growing concerns over these incidents, the effects of spatial confinement during transportation on battery thermal runaway and fire behavior remain insufficiently understood. In this study, considering that batteries during transportation are often in space-limited scenarios, a comparative experiment was conducted to investigate lithium iron phosphate batteries' thermal runaway characteristics and fire hazards in semi-confined space with top openings. The research demonstrates that semi-confined space accelerates the thermal runaway process and exacerbates the fire hazard. Furthermore, as the state of charge increases, the severity of thermal runaway and the associated fire hazard escalate. Notably, as the size of the top opening increases, the battery deflagration transitions from extinction to stable continuous combustion, with gas toxicity initially increasing and then decreasing. This paper emphasizes the critical role of semi-confined space in influencing the fire behavior of lithium-ion batteries. It underscores the importance of effective smoke venting designs to mitigate the risks of battery thermal runaway during transportation. These findings can provide valuable insights for formulating regulations on lithium-ion battery transportation and designing smoke venting systems for transportation containers.

1. Introduction

New energy vehicles are pivotal to transforming the energy structure in the transportation sector and achieving carbon peak and carbon neutrality goals. Lithium-ion power batteries play a crucial role in the market as the power source for new energy vehicles due to their high energy density, long cycle life and environmental friendliness [1]. According to statistical data from the China Automotive Battery Innovation Alliance [2], the installed capacity of lithium-ion power batteries has been growing steadily, and the industry is currently undergoing rapid development. Simultaneously, the volume of transported lithium-ion batteries (LIBs) has risen significantly. However, fire accidents involving LIBs during transportation have become increasingly frequent in recent years. For instance, in January 2022, a truck loaded with lithium iron phosphate batteries (LFP) caught fire on the Beijing-Hong Kong-Macao Expressway in China [3]. In September 2024, a container holding 15 tons of LIBs caught fire at the Port of Montreal, Canada [4]. These accidents resulted in significant economic losses and posed serious health and safety risks to individuals near the accident sites. Consequently, the safety of lithium-ion battery transportation has become an urgent concern.

Fire incidents involving LIBs are typically associated with thermal runaway (TR), which can be triggered by mechanical, electrical or thermal abuse [5]. The mechanisms of TR in LIBs have been extensively studied using techniques such as differential scanning calorimetry (DSC) and accelerating rate calorimetry (ARC) [6,7]. The primary cause is attributed to a series of exothermic side reactions within the battery materials. These reactions generate large amounts of electrolyte vapor and flammable gases, including CO, H_2, CH_4, and C_2H_6 [8,9]. When exposed to an ignition source, these gases can be ignited, releasing significant heat and potentially leading to severe fire and explosion incidents. Numerous studies have investigated the fire behavior and TR characteristics of LIBs. It has been reported that as the state of charge increases, the thermal stability of LIBs decreases, and the fire hazards

---

[*] Corresponding authors.
E-mail addresses: ju.xiaoyu@ustc.edu.cn (X. Ju), yanglz@ustc.edu.cn (L. Yang).

[1] These authors contributed equally to this study and co-first authors.

https://doi.org/10.1016/j.est.2025.117220
Received 17 February 2025; Received in revised form 5 May 2025; Accepted 23 May 2025

intensify [10,11]. Liu et al. [12] compared the safety features of LIBs with different cathode materials using a cone calorimeter. They found that the safety performance of LFP batteries is higher than that of lithium-cobalt-oxide (LCO) batteries and lithium-nickel-manganese-cobalt-oxide (NMC) batteries. However, the vented gases from LFP batteries exhibit a lower explosion limit, higher explosion overpressure, and a larger explosion index compared to those from other types of batteries, indicating a greater potential for explosion risks [13,14]. Moreover, the heating position significantly impacts the internal TR propagation of LIBs. Bottom surface heating leads to severe thermal runaway and jet phenomena [15,16]. Besides, other factors affecting the TR characteristics have also been studied, such as heating power [17], ambient pressure [18,19], mechanical variation [20], and saline water [21,22].

However, the aforementioned studies have primarily been conducted in an open environment. In practical applications, batteries are often transported in confined space, which differs significantly from experimental conditions. As a result, the TR characteristics of LIBs in such confined spaces may vary significantly from those in open spaces. Zhang et al. [23,24] experimentally studied the fire characteristics and TR propagation behavior of LIBs in a confined space with a top plate obstacle. Their research revealed that the extended flames from the top enclosure accelerated the propagation of TR, with flame height and heat flux significantly influenced by the height of the top plate. Zhai et al. [25] investigated the TR behavior of LIBs under inclined ceilings, finding that the inclined design facilitated module cooling. TR propagation can be prevented by adjusting the ceiling angle. Li et al. [26,27] observed that the flame behavior of batteries within a battery enclosure differed from that in an open space. The enclosure delayed the onset of TR but accelerated the propagation speed. Furthermore, the heating position of the enclosure also affected the propagation characteristics. External heat sources led to higher battery temperatures compared to internal ones [27]. Liu et al. [28] studied the TR characteristics and fire risks of NCM811 batteries in both open and closed spaces, finding that the amount of flammable gas in confined spaces was more significant than in open spaces. Their evaluation of the fire toxicity of batteries with different cathode materials in confined space indicated that the fire toxicity of ternary batteries exceeded that of LFP batteries and increased with higher nickel content, confirming catastrophic toxicity in such fire scenarios [29]. These studies demonstrate that TR hazards of LIBs are influenced by confined space. However, most research has focused on scenarios such as battery packs in electric vehicles or battery cabinets in energy storage stations, with limited investigation into the TR characteristics and fire risks of LIBs in confined transportation scenarios. Consequently, these studies do not provide sufficient guidance for the safe transportation of LIBs.

Regulations currently stipulate that the state of charge (SOC) of batteries transported by air must not exceed 30 % [30,31], yet there are no corresponding restrictions on the SOC of batteries by land transportation. Furthermore, when TR occurs in an actual transportation container, the accumulation of large amounts of flammable gases poses a significant explosion hazard. Venting designs are commonly employed to reduce the concentration of flammable gases to mitigate this risk in such confined scenarios [32]. Considering venting designs, this study introduces a semi-confined chamber with a top vent to simulate transportation containers. The differences in TR behavior and characteristics between semi-confined and open spaces were explored to reveal the risks associated with TR in land transportation scenarios. A detailed analysis of the state of charge and top venting size impact on TR behavior and hazards in semi-confined space was also provided. The findings aim to offer reference data for the development of regulations for LIB transportation and the design of venting systems in land transportation containers.

2. Experiments

2.1. Battery samples

In this study, lithium iron phosphate batteries (LFP) were employed. The main components of LFP batteries are a cathode, anode, separator and electrolyte. As the cell with $LiFePO_4$ cathode and graphite anode, the electrolyte is the solution of a lithium salt ($LiPF_6$) and the mixture of organic solvents, including ethylene carbonate (EC), dimethyl carbonate (DMC), and methyl carbonate (EMC). The separator is PP material. Cell's nominal capacity and voltage are 105 Ah and 3.2 V respectively. The battery size is 130 mm long, 36 mm in width and 200 mm in height. Before testing, all experimental batteries were pre-cycled under the constant current/constant voltage mode and then charged to the expected SOCs. After charging, batteries were maintained for 24 h to ensure stability.

2.2. Experimental apparatus

The experimental work is divided into two parts: (1) OS (open space) tests, i.e. the TR tests conducted in open space; (2) SCS (semi-confined space) tests, i.e. the TR tests conducted in semi-confined space. The semi-confined space was a semi-confined steel cabinet with a top vent aimed for exhaust emission and pressure leakage. The dimension of the semi-confined cabinet is 120 × 56 × 56 cm. The front surface of it is equipped with a 50 × 30 cm explosion-proof observation window for observing the experimental phenomena thoroughly.

Fig. 1(a) illustrates the schematic diagram of the experimental platform. The platform consists of a combustion chamber (150 × 150 × 180 cm) and a gas collection and analysis system. The left part is a combustion chamber that is used to place experiments under well-controlled conditions. The right part is the gas collection and analysis system. The fire emissions from batteries were collected entirely through an exhaust hood and conveyed into an analysis system. A Micro differential pressure sensor and thermocouple measured the pipeline's pressure differential (Δp) and gas temperature (T_e). A Servomex 4100 gas analyzer was used to measure the O_2, CO, CO_2, H_2 and SO_2 concentrations. Based on that, the oxygen consumption principle can usually roughly determine combustion's heat release rate (*HRR*) [33]. It is important to note that, on the one hand, due to the strong covalent P—O bonds in the cathode of LFP batteries [34], the oxygen release during the decomposition of cathode is relatively low [35]. On the other hand, *HRR* measured in this study is used to compare the relative values under different conditions. Therefore, the effect of oxygen generated by the battery itself on the *HRR* measurements is neglected.

The arrangements in both OS and SCS tests were almost identical, including the relative distances and positions. The difference was that in the SCS tests, these arrangements were within the combustion cabinet. Fig. 1(b) shows the detailed arrangements in tests; an electric heater was used as the external heating source against the front surface of the battery, and the heating power was 500 W, which is consistent with the heating power commonly adopted in previous studies [10,11,36,37]. Thermal insulating layers were used to reduce heat loss. Steel plates were employed to fasten and clamp the battery. A force sensor between steel plates was introduced to measure the expansion force of the battery due to thermal expansion. Prior to testing, the preloading force was set to 1 kN. The red points in Fig. 1(b) presented thermocouples whose distribution was symmetrical left and right in the space. Two thermocouples were positioned on the middle of the front and back surfaces of the battery. The thermocouples above the battery were arranged every 5 cm. The thermocouples near the top of the space were distributed with the central axis as the dividing line. In the right half, they were spaced every 5, 10, 10, and 15 cm respectively. This study used an electric spark igniter to ignite exhaust gas when batteries were venting. The heater was turned off once the battery triggered TR. Before and after the tests, the battery quality was measured using an electronic scale. The settings of

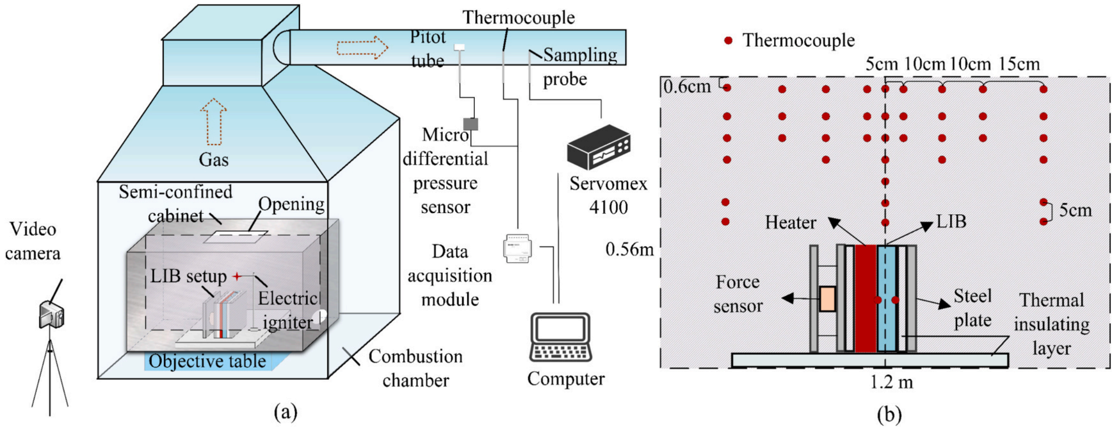

Fig. 1. Schematic diagram of the experimental setup: (a) experimental platform of TR test; (b) detailed arrangements around the battery rig in tests.

experimental conditions are shown in Table 1.

2.3. Error analysis

The error sources related to instrument measurements are exhibited in Table 2, which covers the product model, measuring range and accuracy. The record time of the data acquisition is 1 s. In addition, the unavoidable manufacturing differences among LIBs could not bring about the completely consistent thermal behaviors. To ensure the reliability and reproducibility of the experimental results, each set of experiments in this study was conducted at least twice.

The average values and standard deviations of key parameters across experimental groups are presented in Fig. 2, where T_{max} denotes the maximum surface temperature during TR, t_v represents the time to safety valve opening, m_{loss} indicates the mass loss before and after testing, and F_{max} corresponds to the maximum expansion force measured during TR. As shown in the figure, parameters such as T_{max}, t_v, and m_{loss} exhibited standard deviations <8 %. Furthermore, the maximum expansion force during TR demonstrated good repeatability across all ten experimental groups, with the highest standard deviation remaining <12 %.

Although minor uncertainties are inherent to the experimental process, the relatively low standard deviations across these critical parameters suggest that experimental variability has a limited impact on the overall trends and conclusions drawn in this study. Therefore, the conclusions presented in this paper remain robust and reliable.

Table 1
The settings of the experimental condition.

Group no.	Test no.	SOC	Condition	Opening size
A	#1	100 %	OS	N/A
	#2	100 %	SCS	15*10 cm^2
	#3	50 %	OS	N/A
	#5	50 %	SCS	15*10 cm^2
B	#2	100 %	SCS	15*10 cm^2
	#4	75 %	SCS	15*10 cm^2
	#5	50 %	SCS	15*10 cm^2
	#6	25 %	SCS	15*10 cm^2
C	#1	100 %	OS	N/A
	#2	100 %	SCS	15*10 cm^2
	#7	100 %	SCS	10*10 cm^2
	#8	100 %	SCS	10*5 cm^2
	#9	100 %	SCS	5*5 cm^2
	#10	100 %	SCS	2.5*2.5 cm^2

Note: OS (open space) tests, i.e. the TR tests conducted in open space; SCS (semi-confined space) tests, i.e. the TR tests conducted in semi-confined space.

Table 2
Main uncertainty analysis in instrument measurements.

Device	Product model	Measuring range	Accuracy
Battery test cycler	NEWARE CT-4004-10V100A-NFA	0.005–100 A 0.005–10 V	±0.1 %
Force sensor	Z710	0–29,400 N	±0.03 %
Thermocouples	WRNK-191	0–1200 °C	±0.4 %
Electronic scale	5Y.25.PM	0–25 kg	±0.1 g
Data acquisition	ICPCON I-7017C、7017、7018	N/A	±0.1 %

3. Results and discussion

3.1. Comparison of thermal runaway characteristics in open and semi-confined space

3.1.1. Thermal runaway behavior

Fig. 3 illustrates the TR behavior of LFP batteries at 100 % and 50 % SOC in both open and semi-confined spaces. For LFP batteries at these two SOCs, the overall TR behavior remains essentially consistent. Based on the experimental observations, the process can be categorized into four stages: (I) heating, (II) venting and ignition, (III) stable combustion and jet flame and (IV) decay and extinguishment. At stage I, the batteries were initially heated by the electric heater. As heating continued, the battery surface exhibited slow expansion due to the increasing internal pressure. At stage II, the valve opened, accompanied by the venting of flammable gases when the batteries' internal pressure exceeded the safety valve's opening threshold. In open space, these gases were released upward and formed bright flame in the vertical direction when ignited by an electric igniter at 1564 s and 1510 s for 100 % and 50 % SOC cells respectively. In contrast, violent deflagration occurred in a semi-confined space with flames erupting from the combustion cabinet's opening when the released gases were ignited in 1537 s and 1524 s for these two SOCs respectively. It is speculated that the reason may be that due to the restricted volume of the combustion cabinet, most of the combustible gases released were confined in the space rather than discharged into the atmosphere. The confined gases were ignited instantly upon encountering an ignition source, producing a loud roar. At the start of stage (III), combustion remained stable. As the battery underwent TR, the fire intensified and fluctuated violently, accompanied by increased smoke production. In SCS tests, a substantial amount of smoke accumulates at the top of the semi-confined cabinet and gradually sinks down, with some smoke spilling out through the opening. During TR, two jet fires were formed. Finally, the batteries entered the decay and extinguishment stage.

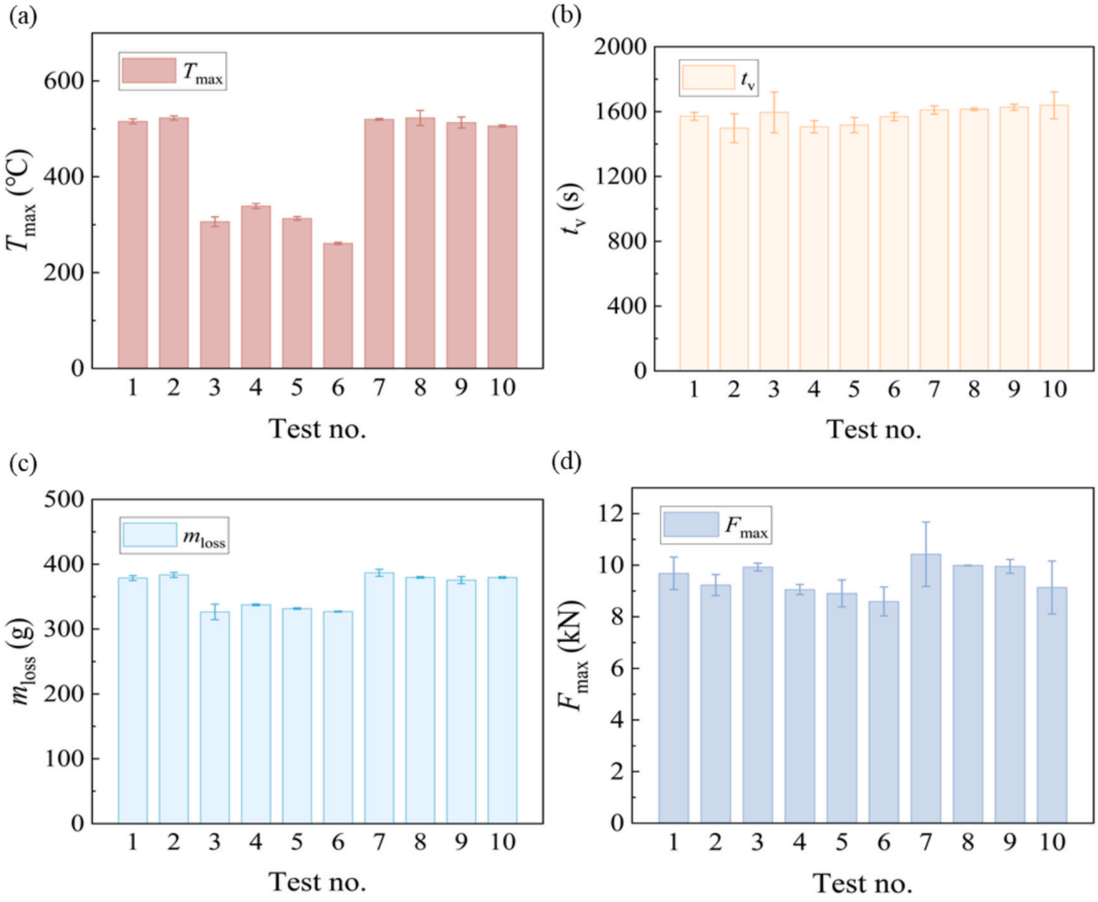

Fig. 2. The error bars of the key parameters.

3.1.2. Surface temperature, voltage and expansion force of batteries

The batteries' surface temperature, voltage, and expansion force are critical parameters for the TR evaluation and early warning of the battery [38]. Fig. 4 illustrates the variation in surface temperature, voltage and expansion force with the time in both tests. During the initial heating stage, the surface temperature increased gradually, and the expansion force exhibited slight fluctuations due to the thermal expansion of the heating plate and battery surface [39]. With continuous heating, the surface temperature rose further, and the expansion force increased significantly, demonstrating its potential as an early warning signal for batteries [40]. As the expansion force reached its first peak, the safety valves opened, corresponding to the time t_v. With the release of a large amount of high-temperature electrolyte vapor and gases, the expansion force dropped sharply, and the front surface temperature slightly decreased by 4–10 °C. Particularly, owing to the deflagration caused by the ignition of combustible gases in SCS tests, the front surface temperature measured of the battery at 100 % SOC reached a peak of 575 °C within 2 s, as shown in Fig. 4(b). The peak temperature corresponds to the flame temperature rather than the battery temperature. With continued external heating and the auto-thermal effect of side reactions in batteries, the separator of the batteries melted, resulting in an internal short circuit (ISC) that manifested as a voltage drop. This study defined t_{ISC} as the moment when the voltage decrease rate approached −0.5 V/s. Subsequently, the TR of the batteries was rapidly triggered, during which the back surface temperature of batteries rose sharply and the voltage dropped to 0 V. Additionally, the chemical reactions occurring inside the battery during TR produced large amounts of gas contributing to another peak in the expansion force. As the TR progressed, the surface temperature of batteries reached a maximum value. Following this, both the temperature and expansion force gradually decreased until the TR reactions ceased.

To facilitate a better comparison of the TR characteristics of batteries in OS tests and SCS tests, the summarized critical data such as the temperature and the onset time of TR (t_{TR}) for 100 % and 50 % SOC batteries is provided in Table 3. The characteristic time and time intervals in SCS tests are significantly shorter than those in OS tests. Specifically, t_{TR} for 100 % and 50 % SOC in SCS tests is advanced by 153 s and 95 s respectively. The time interval between venting and TR, denoted as $\Delta t_{v\text{-}TR}$, is brought forward by 80 s for 100 % SOC batteries, accounting for approximately 50 % of the reduction in the onset time of TR. Indeed, this advancement of the TR critical time in a semi-confined space suggests an increased risk of TR, which brings a more significant challenge to the early warning for battery transportation. The speed $v_{f\text{-}b}$ presents the propagation speed of TR from the front surface to the back front. The calculation method is described below. The symbol "δ" refers to the battery thickness. The results indicate that the spread of TR within an individual cell is more rapid in a semi-confined environment.

$$v_{f-b} = \frac{\delta}{\Delta t_{f-b}} \tag{1}$$

3.1.3. Temperature fields above the batteries at critical times

When the electrolyte vapor and combustible gases released from batteries are ignited, flames form, contributing to the high-temperature zone around batteries. The temperature fields above the battery signify the TR's intensity and significantly affect nearby flammable materials. Fig. 5(a) and (b) show the temperature fields at the time of ignition in both OS and SCS tests. The occurrence of deflagration in SCS tests expands the high-temperature zone. The maximum temperature in OS and SCS tests can reach 167 °C and 399 °C, respectively, surpassing the fire point of corrugated cardboard and timber commonly used as materials

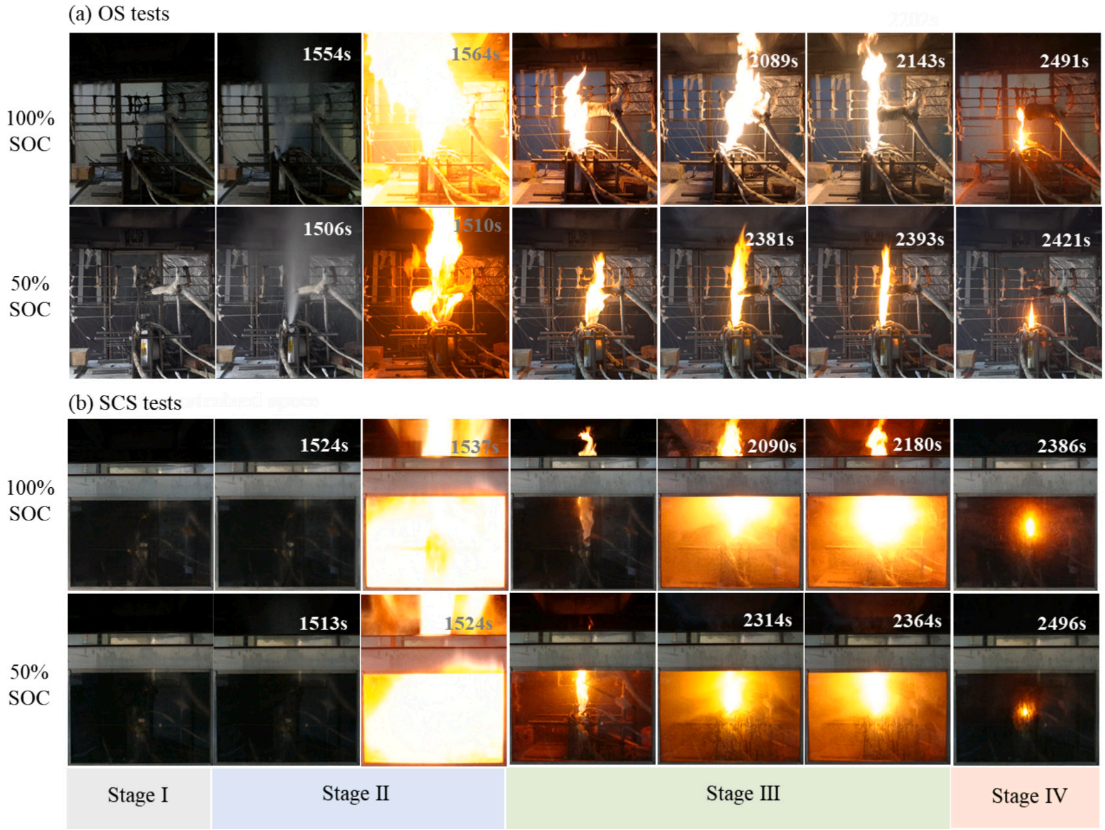

Fig. 3. Thermal runaway behaviors of LFP batteries in open and semi-confined space. (a) OS tests (Test #1 and Test #3); (b)SCS tests (Test #2 and Test #5).

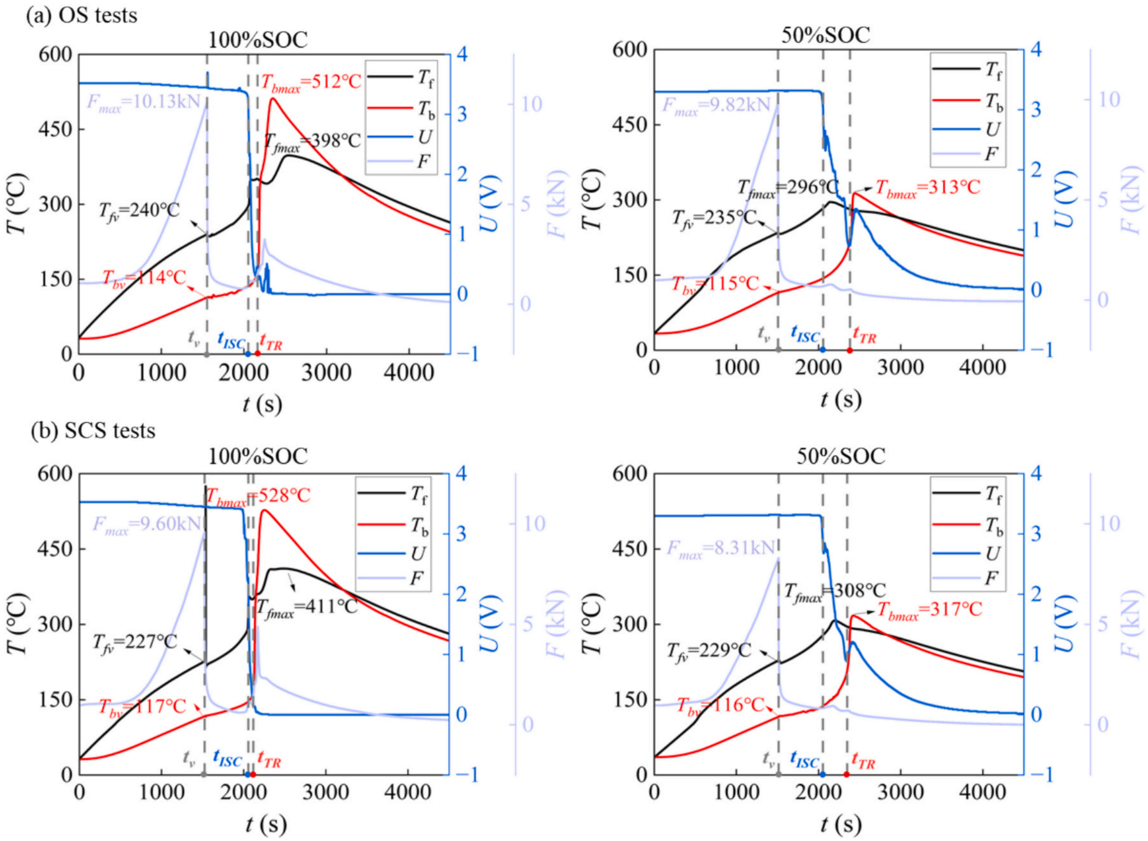

Fig. 4. The surface temperature, voltage and expansion force curves in open and semi-confined space. (a) OS tests; (b) SCS tests.

Table 3
The summarized critical data for 100 % and 50 % SOC batteries in open and semi-confined space.

Condition	OS tests		SCS tests	
	100 %SOC	50 %SOC	100 %SOC	50 %SOC
T_{TR} (°C)	165 ± 4	222 ± 2	164 ± 2	205 ± 2
T_{max} (°C)	516 ± 5	306 ± 10	523 ± 5	313 ± 4
t_{TR} (s)	2211 ± 64	2417 ± 49	2058 ± 72	2322 ± 88
$\Delta t_{\text{v-TR}}$ (s)	640 ± 40	822 ± 77	560 ± 46	805 ± 46
$v_{f\text{-}b}$ (mm/s)	0.39 ± 0.07	N/A	0.48 ± 0.06	N/A

for packaging lithium batteries during transportation. This suggests that if TR causes a fire during transportation, the propagation of TR and the scale of fire will be further aggravated. Fig. 5(c) and (d) show the temperature fields during TR in OS and SCS tests. In SCS tests, the temperature profile exhibits approximate symmetry between the left and right sides. Notably, a clear high-temperature layer is visible at the top of the combustion cabinet, caused by the combined accumulation of high-temperature electrolyte vapor and gases and the heat released by the flame. According to this, it can be inferred that the high-temperature environment formed by the accumulation of heat in the semi-confined space enhances heat transfer between the surrounding environment and the batteries, thereby accelerating the occurrence of TR, as discussed in Section 3.1.2.

3.1.4. Heat release rate

Heat release rate (*HRR*) is one of the key parameters to characterize fire development and evaluate fire hazards quantitatively. Fig. 6 shows three *HRR* peaks corresponding to three venting behaviors during the TR process. The first weak peak caused by ignition after the safe valve opening in both tests is similar. The subsequent two test peaks are attributed to jet fires originating from the two jelly rolls in batteries during TR.

Q_{flame} represents the sum of the heat released by combustible gases from ignition to extinguishment, as defined by the following formula:

$$Q_{\text{flame}} = \int_{t_{ig}}^{t_{ex}} HRR \tag{2}$$

Based on the experimental phenomenon, the flame duration for 100 % SOC batteries in semi-confined space is 1096 s, shorter than the 1210 s observed in open space. This difference is attributed to the fact that 100 % SOC batteries burn more intensely and require more oxygen. In semi-confined space, the limited ventilation restricts the oxygen supply, causing the combustion to proceed more rapidly as the oxygen is consumed quickly. In contrast, for 50 % SOC batteries, the flame duration in semi-confined space is 1001 s, longer than the 1066 s in open space. The possible reason is that 50 % SOC batteries burn less violently and require less oxygen. However, due to the limited oxygen supply in the semi-confined space, the rate of oxygen consumption during combustion is slower, leading to a longer burn time. The calculated average Q_{flame} in semi-confined space is 7.84 MJ and 6.52 MJ for 100 % and 50 % SOC batteries, respectively,which are 0.56 MJ and 0.18 MJ higher than those in open space for these two SOCs respectively. This indicatesa more severe fire hazard in semi-confined space.

3.2. Effects of SOC on TR characteristics and gas production in semi-confined space

In order to comprehensively assess the risks during land transportation, batteries with 25 %, 50 %, 75 % and 100 % SOC selected as representative and typical states of charge were investigated to evalute the impact of SOC on the thermal runaway hazards in semi-confined space.

3.2.1. Temperature characteristics

In the extensive body of research conducted by previous studies [41], thermal runaway is commonly defined as the moment when the rate of temperature increase reaches 1 °C/s. In the present work, although the maximum temperature rise of 25 % SOC batteries is <1 °C/s, the cell temperature increases exponentially, indicating that irreversible physicochemical reactions have occurred within the batteries. Fig. 7 illustrates the variation curves of the back surface temperature and temperature rise rate of batteries at different SOCs within a combustion chamber with a top opening of 15*10 cm^2. It can be observed that surface temperature characteristics are similar while the characteristics of temperature rise rate exhibit slight differences for 100 % SOC batteries. In Fig. 7(b), the temperature rise rate curve shows two distinct peaks for 100 % SOC batteries corresponding to the sequential TR of the two parallel cells within the battery. Table 4 lists the key TR parameters. As SOC increases, the parameters T_{TR} and t_{TR} decrease while the T_{max} and *mass loss ratio* increase, which is consistent with previous studies' findings [28]. Batteries with higher SOC are more prone to trigger TR and generate more heat owing to their high capacity or stored energy.

Fig. 8(a) presents the distribution of temperature fields in semi-confined space at the moment of ignition for batteries with different SOCs. As the SOC of batteries increases, the area occupied by high-temperature regions within the temperature fields significantly expands. Particularly for batteries at 100 % SOC, the temperature in all areas above the batteries is nearly uniformly above 100 °C. Fig. 8(b) shows the temperature cloud map at the moment of TR for batteries, except for the 25 % SOC battery, which is captured when temperature rise rate reaches its peak. From the figure, it is evident that from the onset of battery venting to the occurrence of TR, high-temperature gases and electrolyte vapors that were not promptly expelled through the combustion chamber's opening accumulated above the chamber, forming a distinct layer of high-temperature smoke. For the 25 % SOC battery, the temperature of the smoke layer at the top ranges from 100 to 130 °C, which exerts a certain heating effect on other nearby fresh batteries within the space if batteries being transported. As the SOC increases, the lower bound of the temperature range for the high-temperature smoke layer at the top significantly rises either and the upper bound of that can exceed 300 °C. As the TR progresses, gas generation within the batteries intensifies further, indicating that the heating effect of the high-temperature smoke layer on the surrounding batteries will become more pronounced.

3.2.2. Voltage and expansion force characteristics

In the early stages of TR, the lithium-ion battery's electrical and expansion force characteristics undergo significant changes due to self-discharge of the ISC circuit and the generation of gases within the battery. As shown in Fig. 9(a), the batteries at 100 % SOC experience the earliest voltage drop, followed by a substantial decline. In contrast, the voltage curves of batteries with lower charge levels are more erratic. Fig. 9(b) presents the variation in expansion force over time. The figure shows that the expansion force exhibits three distinct peaks corresponding to venting, ISC, and TR. This is consistent with the findings reported in Reference [38]. Moreover, the third peak expansion force observed in the 100 % SOC batteries during TR is 4.89 kN, more than three times higher than that of batteries with lower charge levels. This suggests that during TR, the rate of gas evaluation in batteries at 100 % SOC is significantly higher than that of batteries with lower charge levels.

3.2.3. Heat release rate and gas production

To characterize the fire hazard of batteries with different SOCs, *HRR* was measured during the experiment, and Q_{flame} was calculated based on Eq. (2). Fig. 10(a) displays three peaks consistent with the expansion force characteristics described earlier. However, it is important to note that at the moment of ignition, the first peak of *HRR* for the 75 % SOC battery is the highest. This can be attributed to the 4-s time interval from

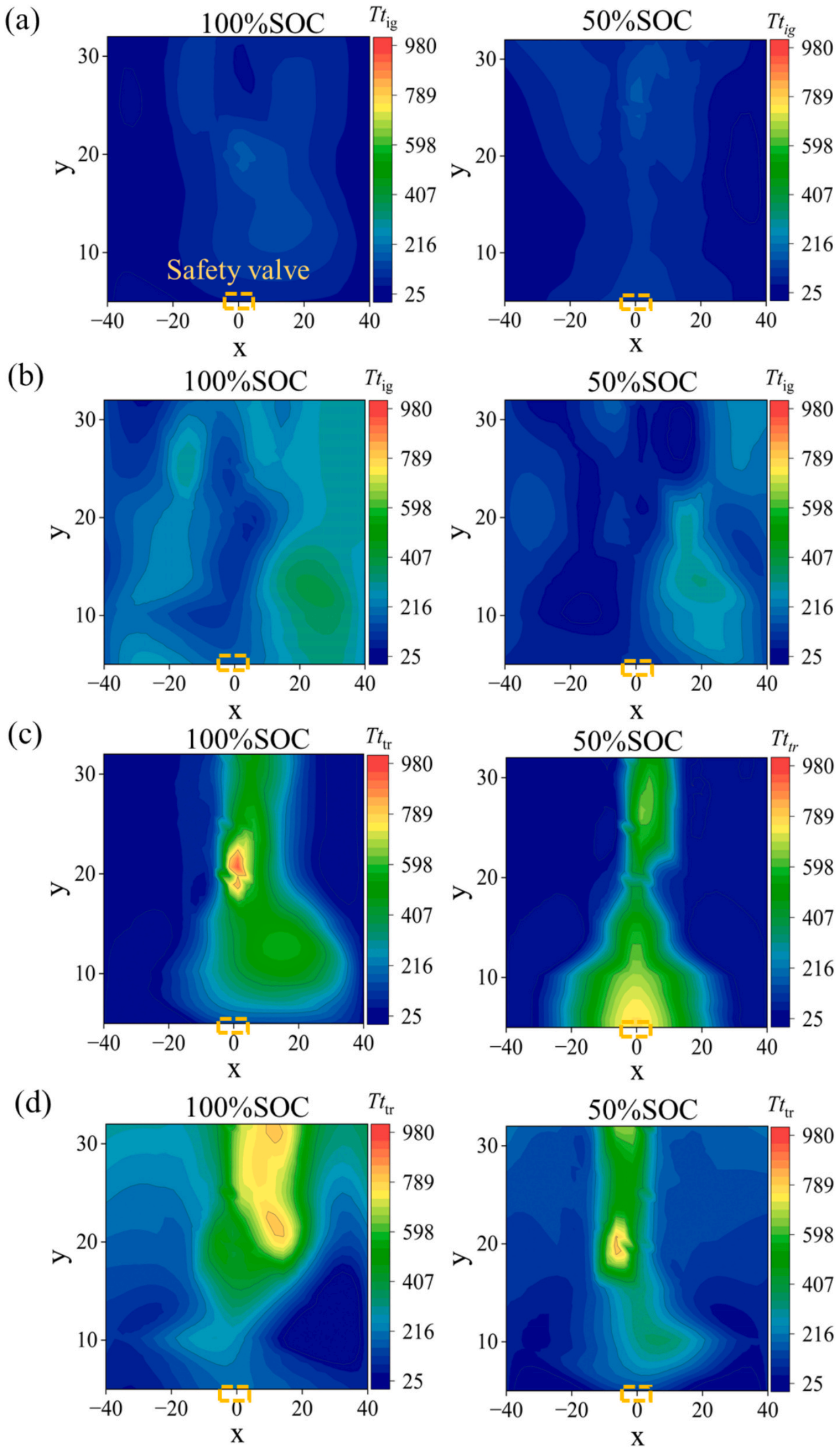

Fig. 5. Temperature fields at the time of ignition and TR. (a) at the time of ignition for OS tests; (b) at the time of ignition for SCS tests; (c) at the time of TR for OS tests; (d) at the time of TR for SCS tests.

battery venting to ignition, which is shorter than the 10-s interval observed in other cases. As a result, less electrolyte vapor and gas are released into the surrounding environment. From the figure, it can be concluded that as the battery charge increases, the peak *HRR* and Q_{flame} also increase, aligning with the trends observed in an open-space environment [10,11].

During TR, batteries also release significant flammable and toxic gases. In order to elucidate the gas generation characteristics in semi-confined space, the gases measured in this study were CO, CO_2, H_2 and SO_2. The variations of gases during the combustion process at

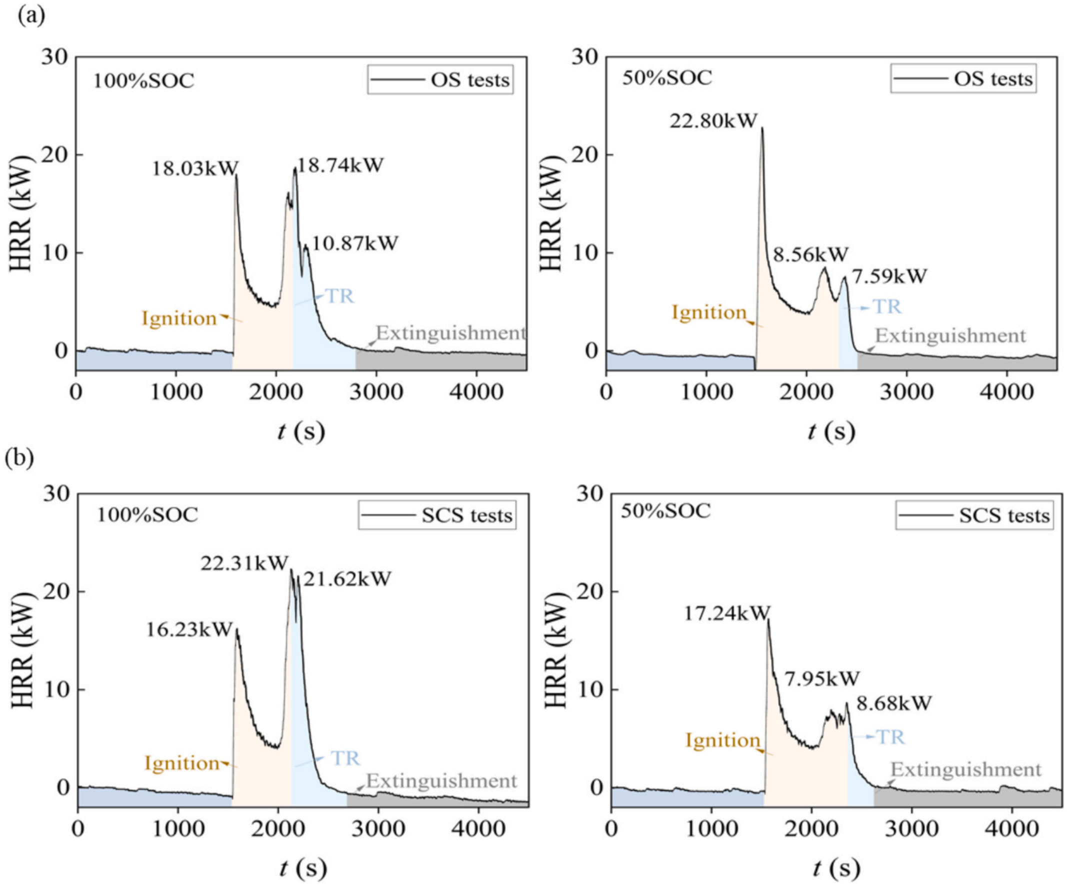

Fig. 6. *HRR* variations for cells in open and semi-confined space. (a) OS tests; (b) SCS tests.

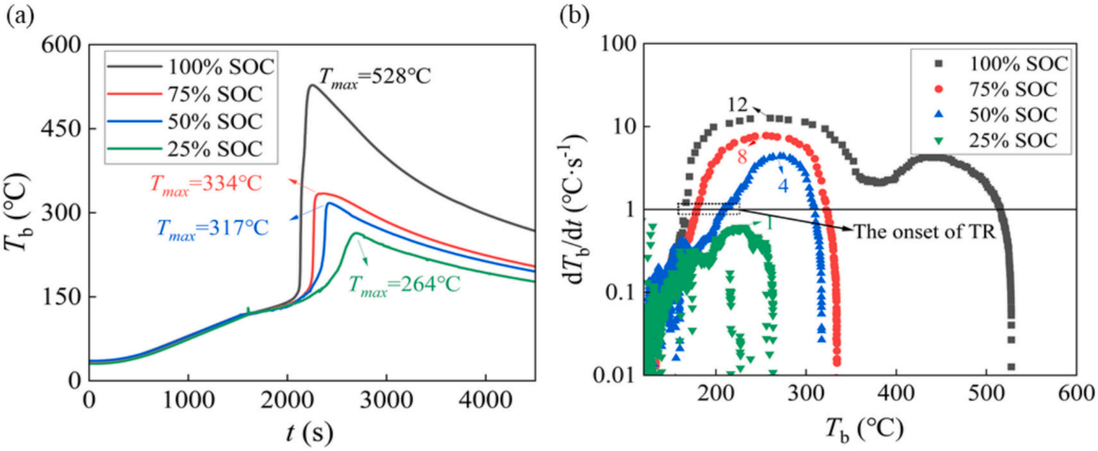

Fig. 7. Surface temperature and temperature rise rate curves at different SOCs in SCS tests. (a) surface temperature variations; (b) temperature rise rate variations.

Table 4
The summarized key parameters for batteries at different SOCs in SCS tests.

SOC	25 %	50 %	75 %	100 %
T_{TR} /°C	N/A	205 ± 2	179 ± 4	164 ± 2
T_{max}/°C	261 ± 2	313 ± 4	339 ± 5	523 ± 4
t_{TR} /s	N/A	2322 ± 88	2209 ± 48	2058 ± 72
Mass loss ratio/ %	16.57 ± 0.07	16.82 ± 0.03	17.08 ± 0.05	19.43 ± 0.20

different SOCs are depicted in Fig. 11(a)~(d).

CO is an explosive and toxic gas generated from the reduction of CO_2 with Li_xC_6 and incomplete combustion. CO_2 originates from the decomposition of the SEI layer, electrolyte decomposition and the complete combustion of gases during TR [42]. As seen in Fig. 11(e), the production of CO and CO_2 increases with SOC, except for the 25 % SOC battery. Interestingly, the production of CO_2 from the 25 % SOC battery is higher than that of the 50 % SOC battery, which can be attributed to the slower reaction rate and the longest duration of combustion observed during TR. As a combustible gas, H_2 is produced by the reaction between the binder and Li_xC_6 and between the electrolyte and the

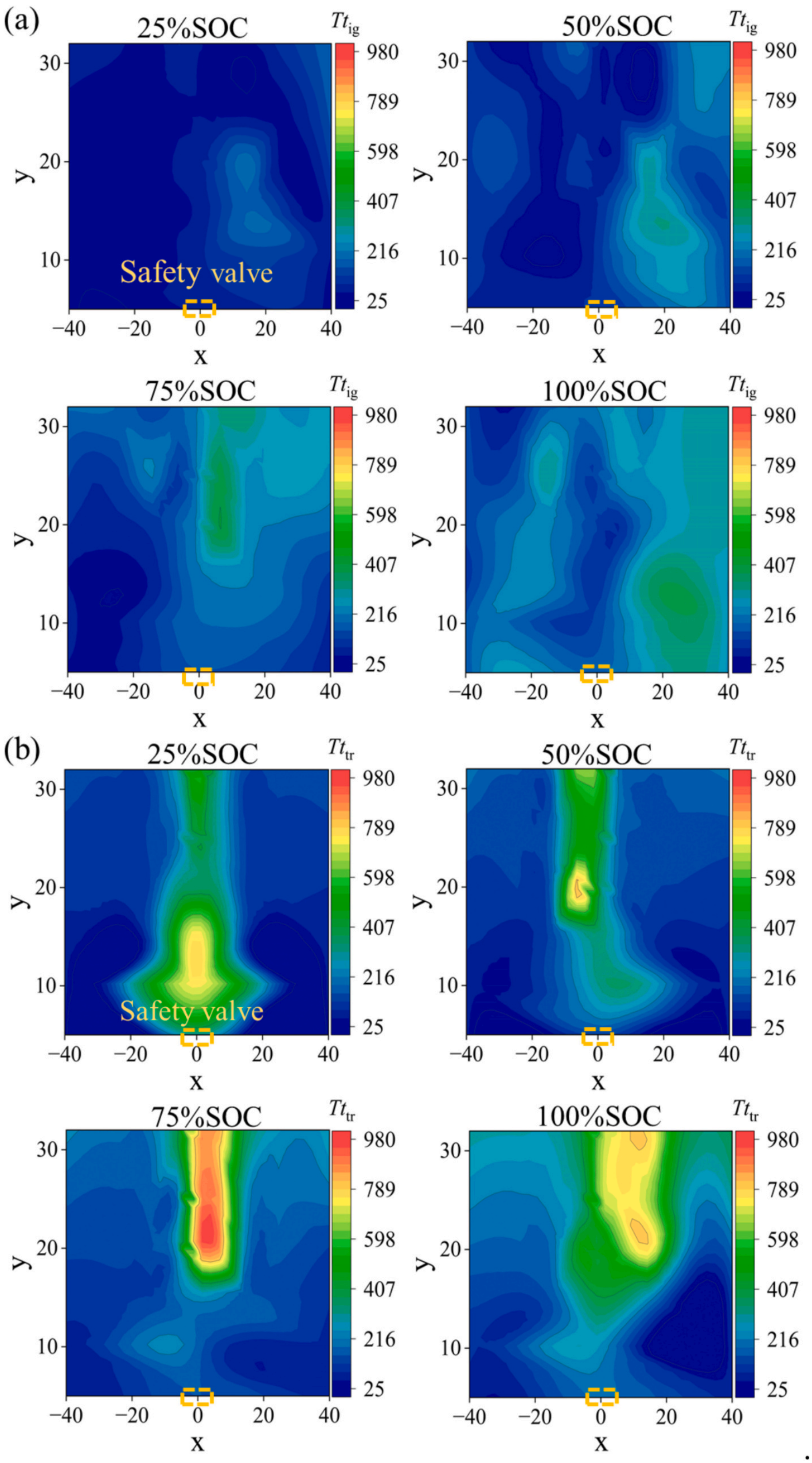

Fig. 8. Temperature fields above the batteries at different SOCs in semi-confined space at critical times. (a) at the time of ignition; (b) at the time of TR.

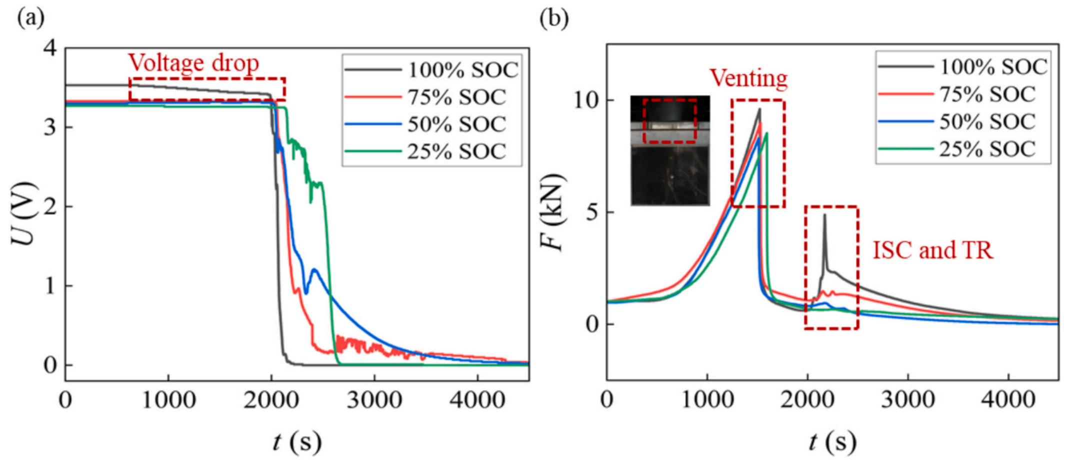

Fig. 9. Voltage and expansion force curves for batteries at different SOCs in semi-confined space. (a) voltage variations; (b) expansion force variations.

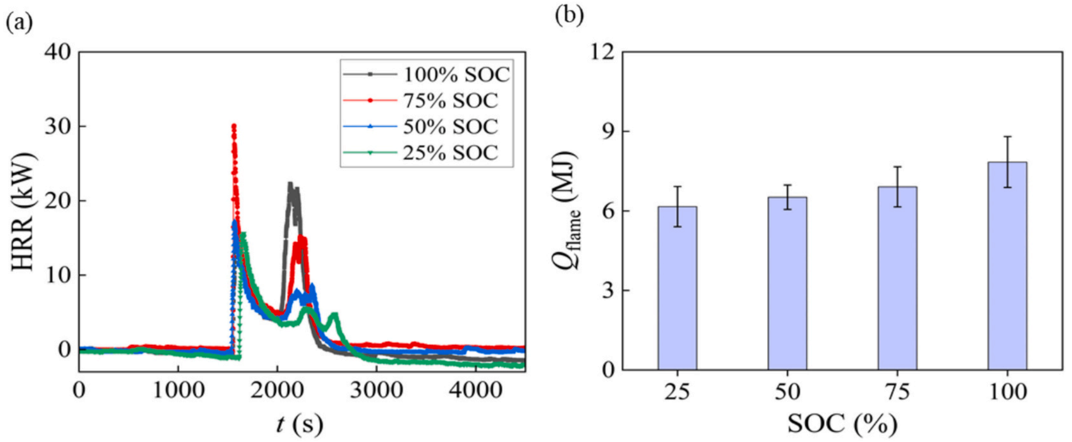

Fig. 10. *HRR* profiles and Q_{flame} for batteries at different SOCs in SCS tests. (a) *HRR* of batteries at different SOCs; (b) Q_{flame} for batteries.

cathode. SO_2 is an irritant gas derived from sulfur-based compounds used as a battery additive to promote the formation of the SEI layer [43]. As exhibited in the figure, the production of H_2 and SO_2 for 100 % SOC battery is the highest, and that is because more Li + intercalating into the anode at higher SOC which enhances these gas production reactions with Li_xC_6.

Among the four gases measured, CO and CO_2 account for the majority of the total gas volume. To evaluate the hazard posed by asphyxiating gases, the Fraction Effective Dose (X_{FED}) developed by ISO 13571 [44] is introduced, calculated with the formula in Eq. (3) and (4):

$$FED = \sum_{t_1}^{t_2} \frac{\varphi_{CO} V_{CO_2}}{35000} \Delta t + \sum_{t_1}^{t_2} \frac{(\varphi_{HCN} V_{CO_2})^{2.36}}{1.2 \times 10^6} \Delta t \tag{3}$$

$$V_{CO_2} = e^{[CO_2]/5} \tag{4}$$

Fig. 11(f) shows the X_{FED} evaluation for the combustion of batteries at different SOCs. It can be observed that asphyxiating gases have a cumulative effect. Once the gases released from batteries in a semi-enclosed space are ignited, the X_{FED} rapidly exceeds the threshold value of 1. As the TR progresses and more gases are released, the X_{FED} surges, especially for the 100 % SOC battery. This indicates that the 100 % SOC battery has the greatest toxic effect, with its maximum X_{FED} being more than twice that of batteries with 25 % SOC.

3.3. Effects of opening size on TR characteristics and gas production in semi-confined space

The design of a top opening in the confined chamber is intended to vent flammable gases and smoke generated by TR batteries during transportation. However, it may also introduce additional oxygen, which could promote combustion. To explore the impact of this top opening on battery TR and combustion, this study examined various opening sizes located at the top center of the combustion chamber, including 2.2*2.5 cm^2, 5*5 cm^2, 10*5 cm^2, 10*10 cm^2 and 15*10 cm^2.

Based on previous analysis, lower SOC batteries typically exhibit a lower risk of TR. However, to account for the worst-case scenario and provide a more comprehensive understanding of the potential hazards during transportation, batteries with 100 % SOC were selected for all tests. Additionally, data from open space tests were included as a comparison group, allowing for a more robust comparative analysis of how the size of the top opening influences the thermal runaway characteristics and gas production of batteries.

3.3.1. Temperature characteristics

During the experiment, temperature data were recorded from both the front and back surfaces of the batteries, as shown in Fig. 12(a) and (b). The patterns of temperature variation are similar across all opening sizes. However, unusual spikes in the temperature curve are observed after the safety valve opens, except for the case with a 2.2*2.5 cm^2 opening and open space. Combining the experimental phenomenon with the temperature curves, it is found that the abnormal peaks within the

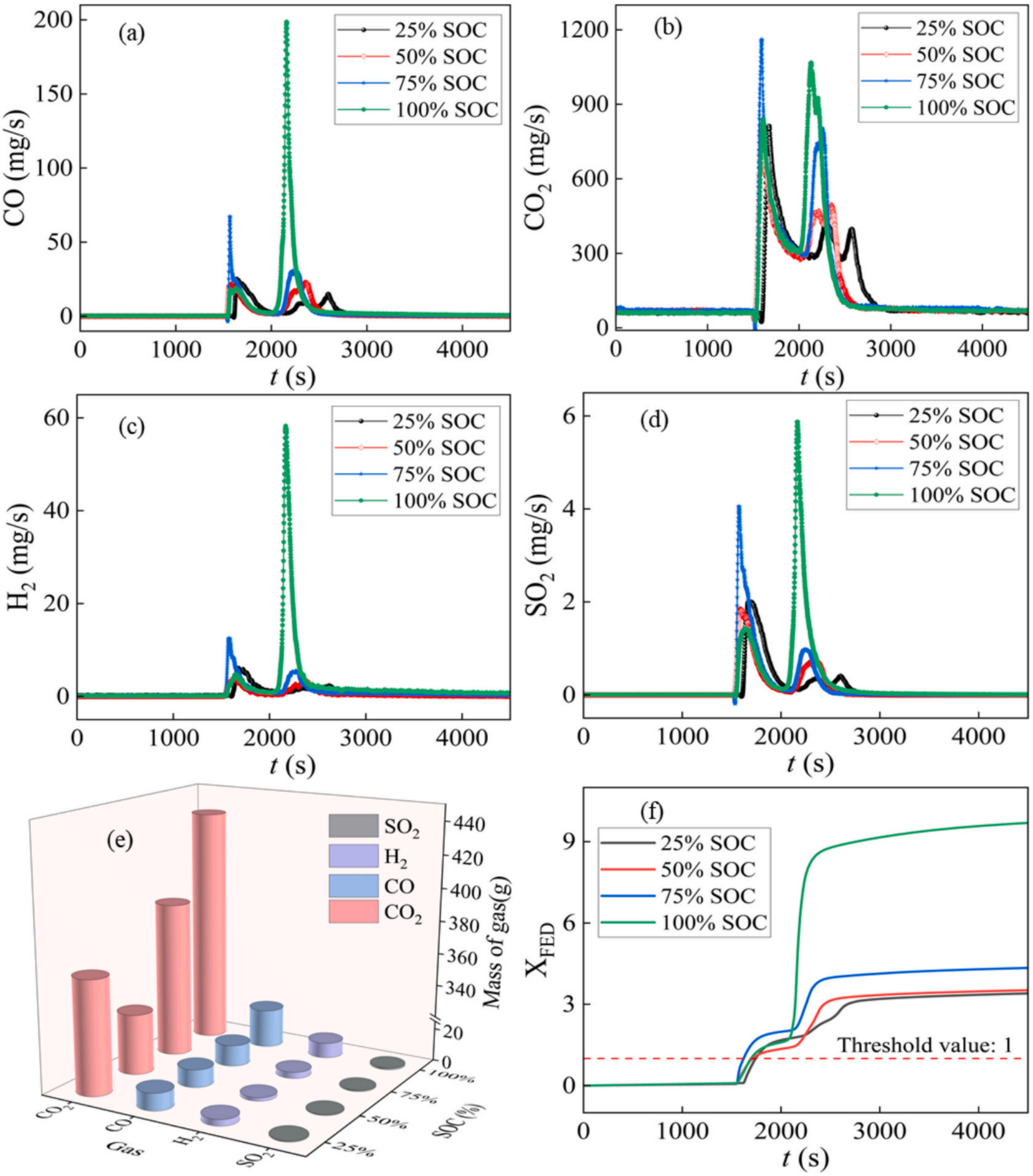

Fig. 11. Analysis of the gas generated at different SOCs in SCS tests. (a) CO; (b) CO_2; (c) H_2; (d) SO_2; (e) gas production of CO, CO_2, H_2 and SO_2 during TR; (f) evolution of X_{FED} of gases.

200–580 °C range correspond to the ignition moments. When the gases emitted by the battery are ignited, deflagration occurs within the partially confined enclosure. The deflagration influences the temperature measurement points on both the front and back surfaces of the battery, resulting in recorded temperatures corresponding to the flame temperature at the time of the explosion. However, this effect dissipates once the deflagration event has concluded. In the case of a 2.5*2.5 cm^2 opening, the emitted gases cannot be ignited, which may be due to the excessive concentration exceeding the flammability limits resulting from the small exhaust vent size.

The opening size affects the TR behavior and influences the characteristic temperature and time intervals associated with TR, as shown in Fig. 12(c) and (d). The onset temperature of TR (T_{TR}) remains unaffected by the opening size, as the intrinsic properties of the battery itself primarily determine it. However, due to the flame effects, the battery's maximum temperature (T_{max}) with a 2.5*2.5cm^2 opening is lower than in other cases. As the opening size increases, the time interval from batteries being heated to triggering TR or reaching T_{max} significantly decreases, with a maximum reduction of over 3 min. Compared with open space, the time intervals between venting and TR of batteries in semi-confined space are lower.

To understand the differences in TR behaviors under various opening sizes, the temperature near the top of the combustion chamber was measured, as shown in Fig. 13. Since no combustion phenomena were observed in the scenario with a 2.5*2.5 cm^2 opening, this case will not be discussed further. The processes are divided into four stages based on venting, TR and the moment of maximum temperature. For the 5*5 cm^2 and 10*5 cm^2 openings, the temperature curves show a single peak of 627 °C and 626 °C, respectively, at the stage II, during which deflagration only lasted for an average of approximately 5–6 s. Afterward, only smoke emission was observed without the presence of flames. In contrast, for the larger openings, the temperature curves exhibit around three peaks. Following the first peak at stage II, the deflagration transitions into stable combustion due to the oxygen supply from the top openings. During this phase, the flame oscillated near the top temperature measurement points 3–5, while the temperature recorded at the

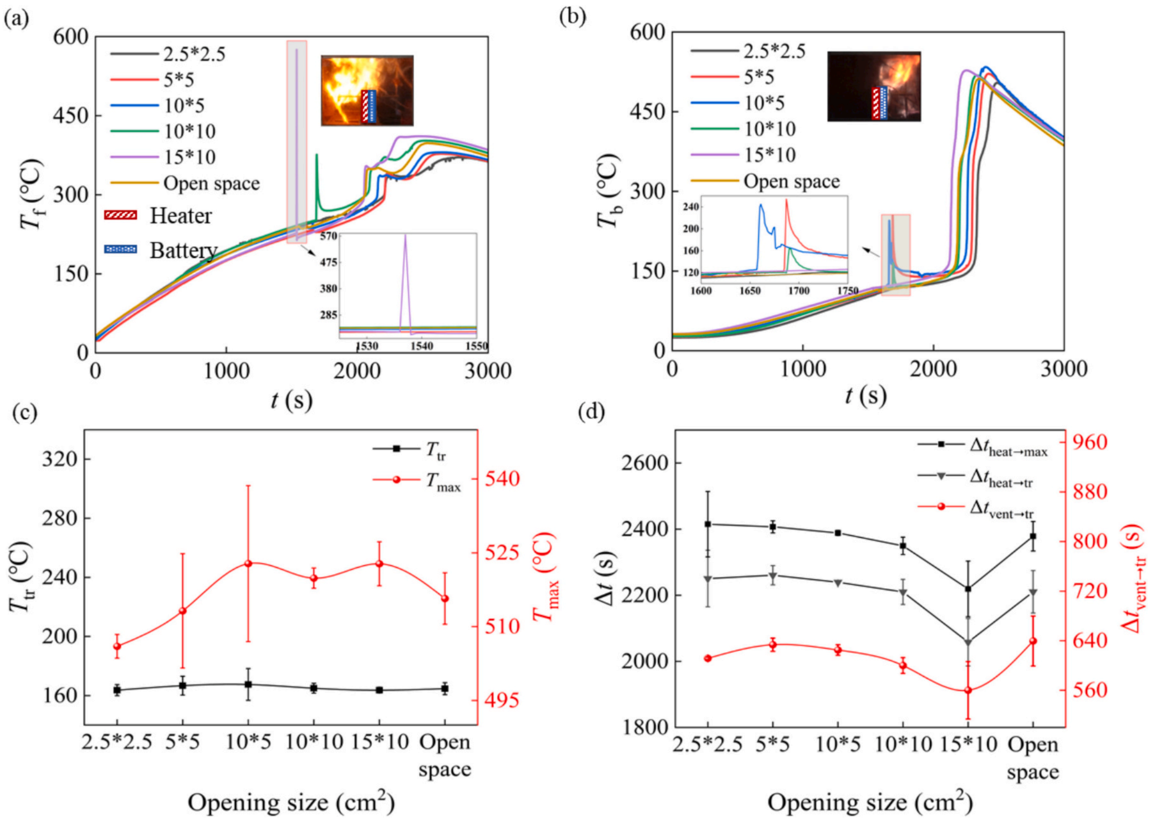

Fig. 12. Cell temperature curves, characteristic temperature and time intervals at different opening sizes. (a) the front surface (heating side) temperature; (b) the back surface (non-heating side) temperature; (c) characteristic temperatures; (d) characteristic time intervals.

remaining points reflected high-temperature smoke. At the end of stage II and during stage III, the temperature curve reached its second and third peaks exceeding 800 °C. The curves fluctuated dramatically during this period as the flame oscillated violently upwards and downwards before and after TR.

To quantitatively assess the impact of opening size on the combustion behavior of batteries, the average temperatures of the smoke accumulated at the top of the semi-confined cabinet during the stages II and III were calculated and analyzed using formulas (5) and (6). Considering the fluctuation of the flame within the several thermocouple ranges, temperature values from these points were excluded from the smoke temperature calculation. Fig. 14 shows that the average smoke temperature in stages II and III for conditions without stable combustion is slightly above 60 °C. Meanwhile, under stable combustion conditions, the average smoke temperatures in the second stage are 183 °C and 150 °C, respectively. Additionally, as the thermal runaway reactions progress, the combustion behavior of batteries becomes most intense during stage III, leading to a rise in the average smoke temperature. As the opening size increases, more oxygen is introduced to support stable combustion, raising the average flue gas temperature. However, when the opening reaches a certain size, it also facilitates the emission of high-temperature flue gases, resulting in a subsequent decrease in the flue gas temperature.

$$\text{At stage II}:\overline{T}_{smoke}=\frac{1}{6}\left(\overline{T_0}+\overline{T_1}+\overline{T_2}+\overline{T_6}+\overline{T_7}+\overline{T_8}\right) \tag{5}$$

$$\text{At stage III}:\overline{T}_{smoke}=\begin{cases}\dfrac{1}{9}\sum\limits_{i=1}^{9}\overline{T_i},\text{without stable combustion}\\[2ex]\dfrac{1}{4}\left(\overline{T_0}+\overline{T_6}+\overline{T_7}+\overline{T_8}\right),\text{stable combustion}\end{cases} \tag{6}$$

3.3.2. *Heat release rate and gas production*

In this study, the combustible gases released from batteries through the 2.5*2.5 cm^2 opening could not be ignited, contributing to the lack of combustion heat generation. For the 5*5 cm^2 and 10*5 cm^2 openings, although significant deflagration occurred, the very short duration of the combustion process resulted in minimal combustion heat. In contrast, for the 10*10 cm^2 and 15*10 cm^2 openings where stable combustion could be achieved, the values of Q_{flame} are 9.20 MJ and 7.84 MJ, respectively, which is considerably higher than that in open space. (See Fig. 15.)The lower combustion heat in the case of a 15*10 cm^2 opening may be attributed to two factors. On one hand, a larger opening facilitates the release of combustible gases from the chamber, reducing the amount of fuel available for combustion. On the other hand, it promotes airflow disturbances, which results in unstable flames and consequently shortens the combustion duration.

Fig. 16(a) illustrates the total mass of each generated gas during the experimental process. For the 2.5*2.5 cm^2 opening, where no visible flame was observed, the production of CO_2 was the lowest. In contrast, for the 10*10 cm^2 and 15*10 cm^2 openings, as well as in open space, where stable combustion was observed, the H_2 yield was significantly

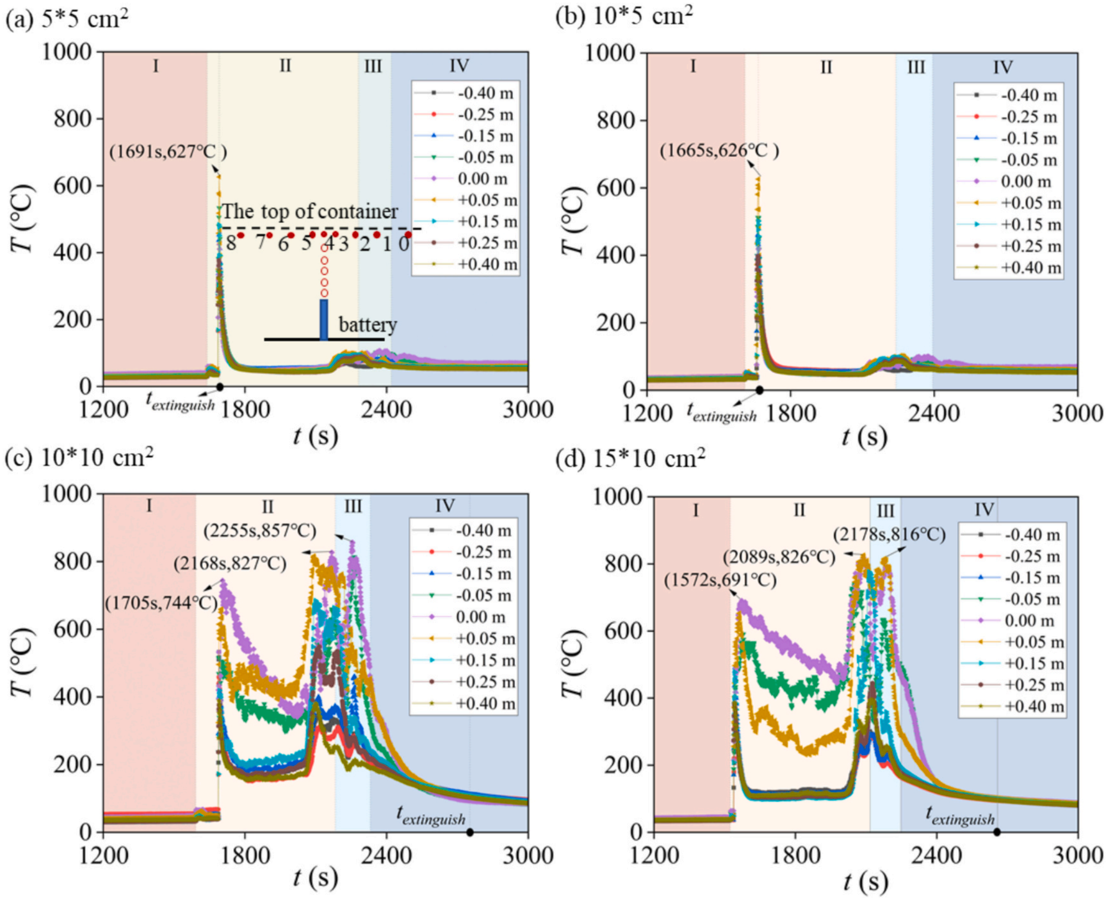

Fig. 13. Horizontal temperature distribution at different opening sizes. (a) 5*5 cm^2; (b) 10*5 cm^2; (c) 10*10 cm^2; (d) 15*10 cm^2.

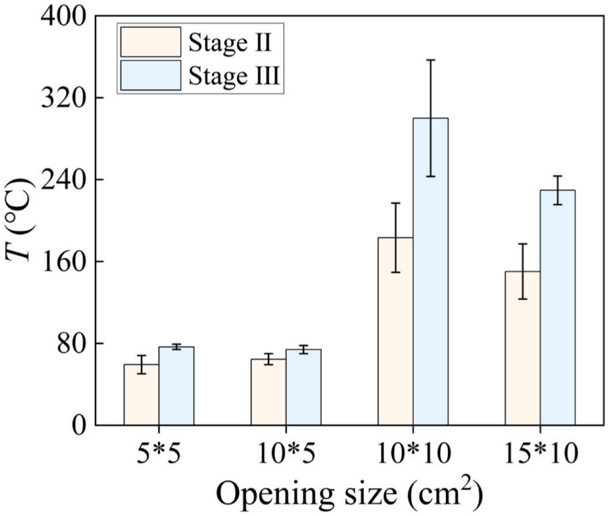

Fig. 14. Average gas temperature at the stage of II and III at different opening sizes.

lower than that under other cases. The corresponding n(CO_2)/n(CO) ratios for these three conditions were 8.58, 11.70, and 42.20, respectively, indicating a progressive improvement in combustion efficiency. However, it should be noted that the CO_2 production under the 10*10 cm^2 and 15*10 cm^2 openings was higher than that observed in open space, which is likely due to greater gas losses to the surrounding environment during open space combustion. Fig. 16(b) delineates the evolution of Fractional Effective Dose (FED) values for asphyxiant gases to facilitate a more sophisticated comparison of the toxicological impact of battery emissions across varying cases. In open space, the gas toxicity is notably lower than that in semi-confined space. With respect to the influence of the opening size in semi-confined space, it is observed that with the increase of the opening sizes, the toxicity of gases initially increases and subsequently decreases. In the case of the 10*5 cm^2 opening where blowout combustion of the battery was followed by flame extinction, the X_{FED} reached its maximum value of 17.60. This is attributed to the fact that the asphyxiant gas considered in the gas toxicity evaluation based on ISO 13571 is CO. According to the experimental data, the highest CO concentration and the lowest combustion efficiency were observed under this condition, resulting in the greatest gas toxicity among all tested scenarios.

3.4. Quantitative assessment of battery thermal runaway and fire hazards in semi-confined space

To comprehensively assess the TR and fire risks and hazards of LIBs in semi-confined space, as a systematic analysis method, the Analytic Hierarchy Process (AHP) is employed to conduct a qualitative and quantitative analysis considering multiple parameters. The analysis process consists of five parts: (1) establishing a hierarchical analysis structure model; (2) constructing judgment matrices; (3) calculating the eigenvector; (4) conducting a consistency check of the rankings; (5) calculating the comprehensive hazard index.

(1) Establishing a hierarchical analysis structure model

The hierarchical analysis structure model involves two dimensions of

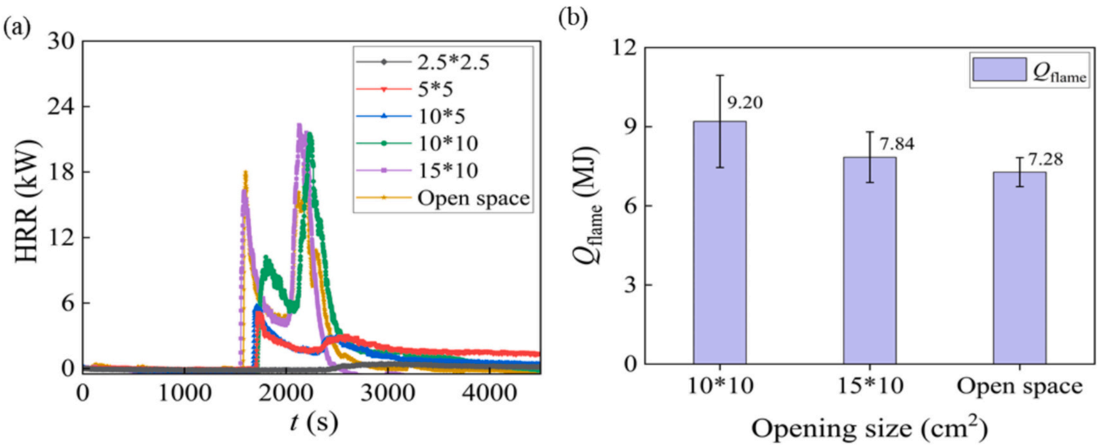

Fig. 15. *HRR* and Q_{flame} for batteries at different opening sizes.

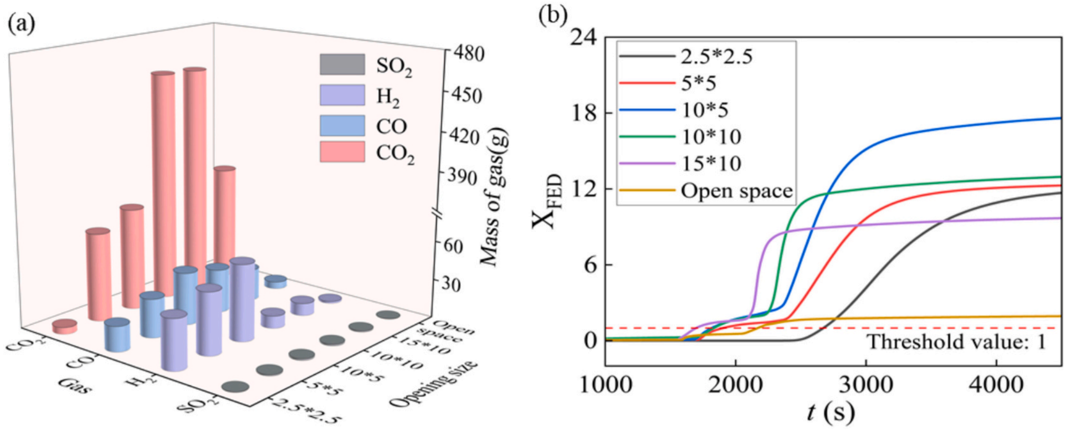

Fig. 16. Analysis of gases generated at different opening sizes. (a) the total mass of CO, CO$_2$, H$_2$ and SO$_2$; (b) evolution of X_{FED} of asphyxiant gases.

risks and hazards associated with LIBs: the TR of batteries and the fire resulting from TR. In the context of battery thermal runaway events, the prevalent characteristic parameters encompass T_{TR}, $T_{\max}$, t_{TR} and T'_{max}. The ranking of TR hazards in the references [45] and [46] is also adopted in this paper: $T_{TR} > T_{max} > T'_{max} > t_{TR}$. In the analysis of traditional fire and battery fire hazards, fire hazards include toxic hazard and heat hazard [47,48]. X_{FED} determines toxic hazard, and heat hazard is characterized by fire growth index (*FGI*), total heat release amount index (*THRI*), and time to ignition (*TTI*) [47,49]. The calculation formula of these parameters is shown in Eqs. (7)–(8) below. Due to the combustion time in semi-confined space far exceeds the 6-min evacuation time allowed in building fires, this paper also adopts the average *HRR* ($\overline{HRR}$) as a substitute for *THRI* and uses the time of safety valve opening (t_v) as a replacement for *TTI* as the reference [46]. Moreover, based on previous fire incidents related to lithium battery transportation [50], the smoke poison poses a more direct threat to the health and safety of nearby personnel during transportation, the toxic hazards resulting from battery thermal runaway should not be underestimated. As a result, the ranking of fire hazards is as follows: $X_{FED} > FGI > \overline{HRR} > t_v$.

$$FGI = pHRR/t_P \tag{7}$$

$$THRI = \log(\overline{HRR} \times 0.36) \tag{8}$$

Table 5
The meanings of ratio scales.

Ratio scale a_{ij}	Meaning
1	Factors *i* and *j* are of equal importance
3	Factor *i* is slightly more important than factor *j*
5	Factor *i* is significantly more important than factor *j*
7	Factor *i* is strongly more important than factor *j*
9	Factor *i* is extremely more important than factor *j*
2,4,6,8	The intermediate importance between the aforementioned judgments
Reciprocal	Compare factor j with factor *i*, $a_{ji} = 1/a_{ij}$

(2) Constructing judgment matrices

Judgment matrices are used to calculate the weights of each evaluation parameter. Each element in the matrix represents the relative importance between two parameters, which is determined by the 1–9 ratio scale method. The ratio scales and their meanings are listed in Table 5. The judgment matrix is an m × m square matrix, as shown in Tables 7 and 8.

$$A = \begin{pmatrix} a_{11} & \cdots & a_{1m} \\ \vdots & \ddots & \vdots \\ a_{m1} & \cdots & a_{mm} \end{pmatrix} \tag{9}$$

(3) Calculating the eigenvector

Methods such as the square root or the sum method are generally used to calculate the eigenvector of a matrix. In this paper, the sum method is adopted, and the calculation is as follows:

$$C = \begin{pmatrix} c_{11} & \cdots & c_{1m} \\ \vdots & \ddots & \vdots \\ c_{m1} & \cdots & c_{mm} \end{pmatrix} \qquad \mathrm{c_{ij}} = a_{ij} \Big/ \sum_{i=1}^{m} a_{ij} \tag{10}$$

$$W = \begin{pmatrix} w_1 \\ \vdots \\ w_m \end{pmatrix} \qquad \mathrm{w_i} = \frac{\sum\limits_{i=1}^{m} c_{ij}}{\sum\limits_{j=1}^{m} \sum\limits_{i=1}^{m} c_{ij}} \tag{11}$$

Among which, w_i represents the weights of each evaluation parameter, as shown in Table 7 and Table 8.

(4) Conducting a consistency check of the rankings

The criterion for consistency is as follows:

$$CR = \frac{CI}{RI} \tag{12}$$

$$CI = \frac{\lambda_{\max} - m}{m - 1} \tag{13}$$

$$\lambda_{\max} = \sum_{i=1}^{m} [(AW)/mW] \tag{14}$$

Among which CI serves as an indicator of consistency, when $CI <$ 0.10, it can be considered that the inconsistency of judgment matrix A is within the acceptable range, and its eigenvector can be used as its weight vector. RI is a measure of random consistency, whose value is obtained from Table 6. $\lambda_{\max}$ It is the maximum eigenvalue of the judgment matrix.

(5) Calculating the comprehensive hazard index

The comprehensive hazard index (CHI) can be calculated based on the equations below, among which TR_i represents the measured value of the evaluation parameter, SV_i is the measured value of the evaluation parameter. If a larger TR_i indicates a smaller risk, $\mathrm{b_i}$ can be calculated using Eq. (15) or Eq. (16). For the convenience of comparative study, this paper selects the measured values in the conditions with an opening size of 15*10 cm^2 as standard values. According to Fig. 17, the ranking of both TR and fire risks for LFP batteries at different SOCs in a semi-confined space is as follows: 100 % SOC > 75 % SOC > 50 % SOC > 25 % SOC; For different opening sizes, the ranking of TR risk is 5*5 cm^2 ≈ 10*5 cm^2 > 10*10 cm^2 > 15*10 cm^2 > open space, the ranking of fire risk is 10*10 cm^2 > 10*5 cm^2 > 15*10 cm^2 > 5*5 cm^2 > open space.

$$CHI = \sum_{i=1}^{m} b_i \tag{15}$$

$$b_i = \left(1 - \frac{TR_i - SV_i}{SV_i}\right) w_i \tag{16}$$

$$b_i = \left(1 - \frac{SV_i - TR_i}{SV_i}\right) w_i \tag{17}$$

Table 6
The values of RI for the judgment matrix.

m	1	2	3	4	5	6	7
RI	0	0	0.58	0.9	1.12	1.24	1.32

Table 7
The judgment matrix of TR.

	T_{TR}	t_{TR}	T_{max}	T'_{max}	w_i
T_{TR}	1	4	2	3	0.467
t_{TR}	1/4	1	1/3	1/2	0.095
T_{max}	1/2	1/3	1	2	0.278
T'_{max}	1/3	2	1/2	1	0.160

$\lambda_{\max}$= 4.031, CI = 0.010, CR = 0.011.

Table 8
The judgment matrix of fire.

	t_v	X_{FED}	FGI	$\overline{HRR}$	w_i
t_v	1	1/4	1/3	1/2	0.095
X_{FED}	4	1	2	3	0.467
FGI	3	1/2	1	2	0.278
$\overline{HRR}$	2	1/3	1/2	1	0.160

$\lambda_{\max}$ = 4.031, CI = 0.010, CR = 0.011.

4. Conclusions

This study experimentally investigated the thermal runaway and fire behavior of prismatic lithium iron phosphate batteries in semi-confined transportation space. The effects of the state of charge (SOC) of batteries and opening sizes of semi-confined cabinets on the cell temperature, smoke temperature distribution, heat release rate and gas toxicity during TR were analyzed in detail. The conclusions of this study are as follows:

1. Compared with open space, LFP batteries in semi-confined space exhibit violent deflagration when vented gases are ignited. Poor heat dissipation conditions and accumulated high-temperature smoke accelerate the onset of TR and expedite its propagation within the cells. Simultaneously, total heat release in SCS tests is higher than in OS tests, indicating higher TR risks during real-world transportation.
2. As the SOC decreases in semi-confined space, the TR risks and gas toxicity decrease. Therefore, it is advisable to transport batteries at lower charge levels during actual transportation.
3. The size of the opening has a minimal impact on the TR characteristics of batteries, yet it exerts a significant influence on their fire behavior. A critical top opening size can transform a battery's deflagration into sustained combustion. When the opening size is smaller than this critical value, enlarging the opening increases total heat release and gas toxicity. On the contrary, when the opening size surpasses the critical threshold, further expansion decreases total heat release and gas toxicity.
4. Based on AHP analysis, it is found that in semi-confined space, both TR and fire risks for LFP batteries increase with the rise in the battery's charge state. Additionally, as the opening size decreases, the risk of TR for the battery escalates. Furthermore, there exists a critical opening size at which the fire risk for the battery reaches its maximum. From a fire risk perspective, smaller openings can be more beneficial to the safe transportation of lithium-ion batteries.

The findings of this study offer valuable insights into the TR risks of LFP batteries during land transportation and highlight the importance of managing the SOC of batteries and optimizing venting designs in semi-confined spaces to mitigate TR and fire hazards. These results can support the development of stricter safety regulations and more effective venting systems for transport containers. However, the study also has certain limitations. The experiments were conducted at the cell level, whereas in real-world scenarios, batteries are typically arranged in

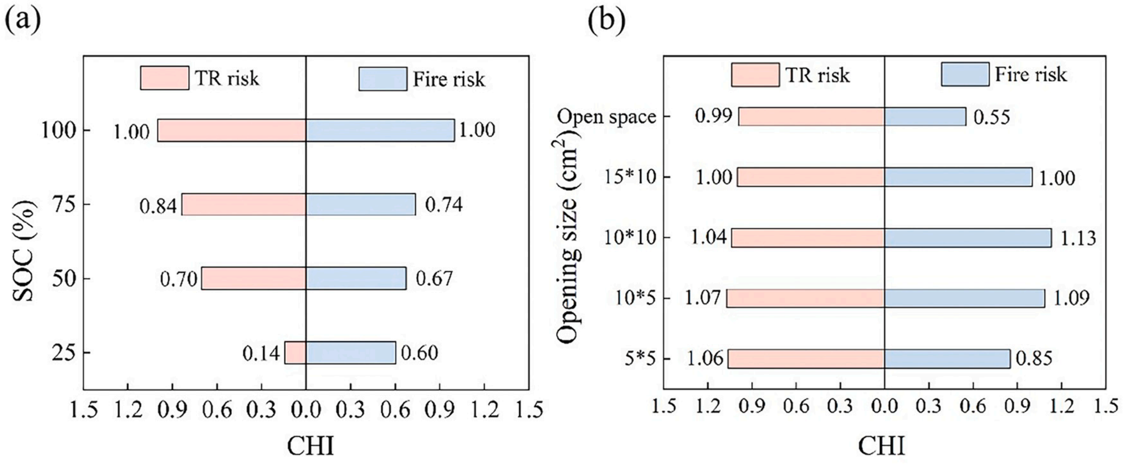

Fig. 17. The comprehensive hazard index (CHI) in different cases of semi-confined space. (a) CHI at different SOCs; (b) CHI at different opening sizes.

modules. Under semi-confined conditions, high-temperature gases and flames may intensify TR propagation across modules. Additionally, the current investigation employed simplified venting designs. Future research will incorporate dynamic ventilation and focus on TR propagation characteristics and heat transfer mechanisms in battery modules under semi-confined configurations.

CRediT authorship contribution statement

Lulu Song: Writing – original draft, Methodology, Investigation, Formal analysis, Data curation, Conceptualization. **Zhizuan Zhou:** Writing – review & editing, Validation, Supervision, Methodology, Investigation, Formal analysis. **Xiaoyu Ju:** Writing – review & editing, Supervision, Resources, Methodology, Funding acquisition. **Boxuan Wang:** Validation, Methodology, Data curation. **Ulises Rojas-Alva:** Writing – review & editing, Validation, Supervision, Funding acquisition. **Xiaodong Zhou:** Validation, Supervision, Methodology. **Lizhong Yang:** Writing – review & editing, Supervision, Methodology, Funding acquisition, Conceptualization.

Declaration of competing interest

The authors declare that they have no known competing financial interests or personal relationships that could have appeared to influence the work reported in this paper.

Acknowledgements

This study was supported by the National High-Level Talent Youth Project (GG2320007006), the National Foreign Experts Program (S20240148), CAS Special Exchange Program (CX2320008006), and USTC Start Research Funding (KY2320000046 & KY2320000055). Additionally, this study has been supported by funding received from the European Union's Horizon 2020 Research and Innovation Programme under Grant Agreement No. 952395.

Data availability

The authors are unable or have chosen not to specify which data has been used.

References

[1] J. Chen, Carbon neutrality: toward a sustainable future, Innov 2 (2021) 100127, https://doi.org/10.1016/j.xinn.2021.100127.

[2] December 2024 Power Battery Monthly Information. https://www.ne-time.cn/web/article/35168, 2025.

[3] Breaking news! A truck loaded with lithium batteries catches fire on the highway. https://www.thepaper.cn/newsDetail_forward_16292141, 2022.

[4] A lithium battery fire sent toxic gas over Montreal. Are we ready for such emergencies?. https://www.cbc.ca/news/canada/montreal/montreal-lithium-battery-fire-concerns-1.7336652?cmp=rss, 2024.

[5] P. Huang, G. Hu, Z. Yong, B. Mao, Z. Bai, Fire risk assessment of battery transportation and storage by combining fault tree analysis and fuzzy logic, Journal of Loss Prevention in the Process Industries. 77 (2022) 104774, https://doi.org/10.1016/j.jlp.2022.104774.

[6] J. Wen, Y. Yu, C. Chen, A review on lithium-ion batteries safety issues: existing problems and possible solutions, Mater. Express 2 (2012) 197–212, https://doi.org/10.1166/mex.2012.1075.

[7] X. Feng, S. Zheng, D. Ren, X. He, L. Wang, H. Cui, et al., Investigating the thermal runaway mechanisms of lithium-ion batteries based on thermal analysis database, Appl. Energy 246 (2019) 53–64, https://doi.org/10.1016/j.apenergy.2019.04.009.

[8] Q. Zhang, T. Liu, C. Hao, Y. Qu, J. Niu, Q. Wang, et al., In situ Raman investigation on gas components and explosion risk of thermal runaway emission from lithium-ion battery, Journal of Energy Storage. 56 (2022) 105905, https://doi.org/10.1016/j.est.2022.105905.

[9] Q. Zhang, J. Niu, Z. Zhao, Q. Wang, Research on the effect of thermal runaway gas components and explosion limits of lithium-ion batteries under different charge states, Journal of Energy Storage. 45 (2022) 103759, https://doi.org/10.1016/j.est.2021.103759.

[10] P. Liu, C. Liu, K. Yang, M. Zhang, F. Gao, B. Mao, et al., Thermal runaway and fire behaviors of lithium iron phosphate battery induced by over heating, Journal of Energy Storage. 31 (2020) 101714, https://doi.org/10.1016/j.est.2020.101714.

[11] P. Liu, Y. Li, B. Mao, M. Chen, Z. Huang, Q. Wang, Experimental study on thermal runaway and fire behaviors of large format lithium iron phosphate battery, Appl. Therm. Eng. 192 (2021) 116949, https://doi.org/10.1016/j.applthermaleng.2021.116949.

[12] C. Liu, W. Shen, X. Liu, Y. Chen, C. Ding, Q. Huang, Research on thermal runaway process of 18650 cylindrical lithium-ion batteries with different cathodes using cone calorimetry, Journal of Energy Storage. 64 (2023) 107175, https://doi.org/10.1016/j.est.2023.107175.

[13] H. Wang, H. Xu, Z. Zhang, Q. Wang, C. Jin, C. Wu, et al., Fire and explosion characteristics of vent gas from lithium-ion batteries after thermal runaway: a comparative study, eTransportation 13 (2022) 100190, https://doi.org/10.1016/j.etran.2022.100190.

[14] A.R. Baird, E.J. Archibald, K.C. Marr, O.A. Ezekoye, Explosion hazards from lithium-ion battery vent gas, J. Power Sources 446 (2020) 227257, https://doi.org/10.1016/j.jpowsour.2019.227257.

[15] Z. Zhou, X. Ju, X. Zhou, L. Yang, B. Cao, A comprehensive study on the impact of heating position on thermal runaway of prismatic lithium-ion batteries, J. Power Sources 520 (2022) 230919, https://doi.org/10.1016/j.jpowsour.2021.230919.

[16] Z. Huang, Y. Yu, Q. Duan, P. Qin, J. Sun, Q. Wang, Heating position effect on internal thermal runaway propagation in large-format lithium iron phosphate battery, Appl. Energy 325 (2022) 119778, https://doi.org/10.1016/j.apenergy.2022.119778.

[17] Z. Zhou, X. Zhou, Y. Peng, L. Li, J. Cao, L. Yang, et al., Quantitative study on the thermal failure features of lithium iron phosphate batteries under varied heating powers, Appl. Therm. Eng. 185 (2021) 116346, https://doi.org/10.1016/j.applthermaleng.2020.116346.

[18] M. Chen, D. Ouyang, J. Weng, J. Liu, J. Wang, Environmental pressure effects on thermal runaway and fire behaviors of lithium-ion battery with different cathodes and state of charge, Process Safety and Environmental Protection. 130 (2019) 250–256, https://doi.org/10.1016/j.psep.2019.08.023.

[19] S. Xie, L. Ren, X. Yang, H. Wang, Q. Sun, X. Chen, et al., Influence of cycling aging and ambient pressure on the thermal safety features of lithium-ion battery, J. Power Sources 448 (2020), https://doi.org/10.1016/j.jpowsour.2019.227425.

[20] Q. Zhang, D. Li, J. Yang, Effect of vibration on cyclic and thermal runaway characteristics of lithium ion batteries, J. Beijing Univ. Aeronaut. Astronaut. (2023), https://doi.org/10.13700/j.bh.1001-5965.2023.0267.

[21] C. Tao, Q. Ye, C. Wang, Y. Qian, C. Wang, T. Zhou, et al., An experimental investigation on the burning behaviors of lithium ion batteries after different immersion times, J. Clean. Prod. (2020) 242, https://doi.org/10.1016/j.jclepro.2019.118539.

[22] Z. Wang, Q. Zhao, W. An, B. Shi, Z. Li, H. Liu, Thermal runaway characteristics of NaCl salt solution-immersed 18650 batteries: impacts of concentration and state of charge, Journal of Energy Storage. 74 (2023) 109369, https://doi.org/10.1016/j.est.2023.109369.

[23] Y. Zhang, D. Kong, P. Ping, H. Zhao, X. Dai, X. Chen, Effect of a plate obstacle on fire behavior of 18650 lithium ion battery: an experimental study, J. Energy Storage 54 (2022), https://doi.org/10.1016/j.est.2022.105283.

[24] Y. Zhang, H. Zhao, G. Wang, X. Gao, P. Ping, D. Kong, et al., Effect of flame heating on thermal runaway propagation of lithium-ion batteries in confined space, Journal of Energy Storage. 78 (2024) 110052, https://doi.org/10.1016/j.est.2023.110052.

[25] H. Zhai, M. Chi, J. Li, D. Li, Z. Huang, Z. Jia, et al., Thermal runaway propagation in large format lithium ion battery modules under inclined ceilings, Journal of Energy Storage 51 (2022) 104477, https://doi.org/10.1016/j.est.2022.104477.

[26] Z. Li, Y. Guo, P. Zhang, Effects of the battery enclosure on the thermal behaviors of lithium-ion battery module during thermal runaway propagation by external-heating, Journal of Energy Storage 48 (2022) 104002, https://doi.org/10.1016/j.est.2022.104002.

[27] Z. Li, P. Zhang, R. Shang, Effects of heating position on the thermal runaway propagation of a lithium-ion battery module in a battery enclosure, Appl. Therm. Eng. 222 (2023) 119830, https://doi.org/10.1016/j.applthermaleng.2022.119830.

[28] P. Liu, H. Sun, Y. Qiao, S. Sun, C. Wang, K. Jin, et al., Experimental study on the thermal runaway and fire behavior of $LiNi_{0.8}Co_{0.1}Mn_{0.1}O_2$ battery in open and confined spaces, Process Saf. Environ. Prot. 158 (2022) 711–726, https://doi.org/10.1016/j.psep.2021.12.056.

[29] P. Liu, C. Wang, S. Sun, G. Zhao, X. Yu, Y. Hu, et al., Understanding the influence of the confined cabinet on thermal runaway of large format batteries with different chemistries: a comparison and safety assessment study, J. Energy Storage 74 (2023), https://doi.org/10.1016/j.est.2023.109337.

[30] International Air Transport Association (IATA), Dangerous Goods Regulations, 66 ed., International Air Transport Association, Montreal, QC, Canada, 2025.

[31] MH/T 1020-2018, Specification for transport of lithium batteries by air. https://www.caac.gov.cn/XXGK/XXGK/BZGF/HYBZ/201904/P020240719352999317163.pdf, 2018.

[32] J. Conzen, S. Lakshmipathy, A. Kapahi, S. Kraft, M. DiDomizio, Lithium ion battery energy storage systems (BESS) hazards, J. Loss Prev. Process Ind. 81 (2023) 104932, https://doi.org/10.1016/j.jlp.2022.104932.

[33] C. Huggett, Estimation of rate of heat release by means of oxygen consumption measurements, Fire Mater. 4 (1980) 61–65, https://doi.org/10.1002/fam.810040202.

[34] G. Chen, T.J. Richardson, Thermal instability of olivine-type LiMnPO4 cathodes, J. Power Sources 195 (2010) 1221–1224, https://doi.org/10.1016/j.jpowsour.2009.08.046.

[35] A.O. Said, C. Lee, S.I. Stoliarov, Experimental investigation of cascading failure in 18650 lithium ion cell arrays: impact of cathode chemistry, J. Power Sources 446 (2020) 227347, https://doi.org/10.1016/j.jpowsour.2019.227347.

[36] S. Wang, L. Song, C. Li, J. Tian, K. Jin, Q. Duan, et al., Experimental study of gas production and flame behavior induced by the thermal runaway of 280 Ah lithium iron phosphate battery, Journal of Energy Storage 74 (2023) 109368, https://doi.org/10.1016/j.est.2023.109368.

[37] Z. Zhou, M. Li, X. Zhou, L. Li, X. Ju, L. Yang, Investigating thermal runaway triggering mechanism of the prismatic lithium iron phosphate battery under thermal abuse, Renew. Energy 220 (2024) 119674, https://doi.org/10.1016/j.renene.2023.119674.

[38] K. Li, J. Li, X. Gao, Y. Lu, D. Wang, W. Zhang, et al., Effect of preload forces on multidimensional signal dynamic behaviours for battery early safety warning, J. Energy Chem. 92 (2024) 484–498, https://doi.org/10.1016/j.jechem.2023.12.045.

[39] Z. Jia, L. Song, W. Mei, Y. Yu, X. Meng, K. Jin, et al., The preload force effect on the thermal runaway and venting behaviors of large-format prismatic LiFePO4 batteries, Appl. Energy 327 (2022) 120100, https://doi.org/10.1016/j.apenergy.2022.120100.

[40] S. Chen, X. Wei, G. Zhang, X. Rui, C. Xu, X. Feng, et al., Active and passive safety enhancement for batteries from force perspective, Renew. Sustain. Energy Rev. 187 (2023) 113740, https://doi.org/10.1016/j.rser.2023.113740.

[41] X. Feng, M. Fang, X. He, M. Ouyang, L. Lu, H. Wang, et al., Thermal runaway features of large format prismatic lithium ion battery using extended volume accelerating rate calorimetry, J. Power Sources 255 (2014) 294–301, https://doi.org/10.1016/j.jpowsour.2014.01.005.

[42] D. Kong, H. Lv, P. Ping, G. Wang, A review of early warning methods of thermal runaway of lithium ion batteries, Journal of Energy Storage 64 (2023) 107073, https://doi.org/10.1016/j.est.2023.107073.

[43] S.S. Zhang, A review on electrolyte additives for lithium-ion batteries, J. Power Sources 162 (2006) 1379–1394, https://doi.org/10.1016/j.jpowsour.2006.07.074.

[44] I.O. Standardization, Life-threatening components of fire: guidelines for the estimation of time to compromised tenability in fires, ISO (2012) 13571.

[45] Z. Wang, S. Chen, X. He, C. Wang, D. Zhao, A multi-factor evaluation method for the thermal runaway risk of lithium-ion batteries, Journal of Energy Storage. 45 (2022) 103767, https://doi.org/10.1016/j.est.2021.103767.

[46] D. Jie, C. Baohui, L. Jiazheng, Z. Tiannian, W. Chuanping, Thermal runaway and combustion characteristics, risk and hazard evaluation of lithium-iron phosphate battery under different thermal runaway triggering modes, Appl. Energy 368 (2024) 123451, https://doi.org/10.1016/j.apenergy.2024.123451.

[47] B. Yu, M. Liu, L. Lu, X. Dong, W. Gao, K. Tang, Fire hazard evaluation of thermoplastics based on analytic hierarchy process (AHP) method, Fire Mater. 34 (2010) 251–260, https://doi.org/10.1002/fam.1019.

[48] Y. Peng, L. Yang, X. Ju, B. Liao, K. Ye, L. Li, et al., A comprehensive investigation on the thermal and toxic hazards of large format lithium-ion batteries with LiFePO4 cathode, J. Hazard. Mater. 381 (2020) 120916, https://doi.org/10.1016/j.jhazmat.2019.120916.

[49] J. Cao, X. Ju, Y. Peng, X. Zhou, Y. Hu, L. Li, et al., Experimental study on fire hazard of LiCoO2-based lithium-ion batteries with gel electrolyte using a cone calorimeter, Journal of Energy Storage. 32 (2020) 101884, https://doi.org/10.1016/j.est.2020.101884.

[50] Lockdown notice issued for residents near Port of Montreal due to lithium battery fire. https://www.ctvnews.ca/montreal/article/lockdown-notice-issued-for-residents-near-port-of-montreal-due-to-lithium-battery-fire/, 2024.